Mech. Sci., 17, 699–712, 2026
https://doi.org/10.5194/ms-17-699-2026

Mechanical Sciences
Open Access

Multi-objective optimization study on the structure of self-excited oscillating pulse cavitation jet nozzles in submerged environments

Jinhui Fan[1,2], Hao Peng[1,2], Ke Liu[1,2], Yuan Gao[3], Liang Zhang[3], and Changkun He[3]

[1]CNPC Engineering Technology R&D Company Limited, Beijing 102206, China
[2]National Engineering Research Center of Oil & Drilling and Completion Technology, Beijing 102206, China
[3]School of Mechanical Engineering, Southwest Petroleum University, Chengdu Sichuan 610500, China

Correspondence: Yuan Gao (1435422371@qq.com)

Received: 8 December 2025 – Revised: 17 June 2026 – Accepted: 18 June 2026 – Published: 3 July 2026

Abstract. Mud circulation tanks efficiently remove accumulated mud cake and impurities from the tank, stabilizing drilling fluid performance and directly ensuring drilling safety and efficiency. Automatic cleaning of these tanks is critical for modern drilling operations. This paper designs an integrated optimization system applied to self-excited cavitation jet nozzles to enhance their comprehensive cleaning performance on mud tanks in submerged environments. Using inlet radius, cavity diameter, cavity length, and lower-nozzle diameter as design variables and pressure peak, amplitude, and frequency as objective variables, orthogonal experiments and range analysis were conducted to obtain optimized structural parameters under orthogonal analysis and identify key structural variables. Subsequently, the discrete optimization space, constructed from key structural parameters, was mapped to the continuous optimization space of the machine learning model. A multi-objective particle swarm optimization algorithm was employed to obtain the Pareto front. Finally, the optimal structures were ranked using the technique for order preference by similarity to an ideal solution method. Compared to the orthogonal analysis results, the optimized structure achieved improvements of 69.79 %, 78.60 %, and 11.77 % in pressure peak, amplitude, and frequency, respectively. Overall cleaning capacity increased by 77.39 %. Simulations of the optimal structure obtained through the integrated optimization system revealed that the nozzle's optimal configuration generates a distinct pulsed cavitation jet. The cavitation zone within the nozzle cavity undergoes periodic contraction and expansion over time, validating the optimization results. The self-excited cavitation jet nozzle structure designed via the integrated optimization system significantly enhances its overall cleaning performance, providing an effective solution for the automatic cleaning of mud circulation tanks.

1 Introduction

The mud circulation tank is an indispensable piece of equipment in drilling operations. During use, drilling mud circulating within the tank inevitably generates residues and deposits. The resulting solid mud cake significantly reduces the tank's effective volume, markedly impacting mud mixing and circulation efficiency (Gonzalez et al., 2021; Ma et al., 2023). Cleaning the mud circulation tank can effectively prevent these issues. However, existing cleaning methods typically rely on manual scrubbing or high-pressure water jetting. High-pressure water jetting has limited cleaning capability, while manual cleaning is inefficient (Kang et al., 2021; Fang et al., 2023). Therefore, there is a need to develop a new technology for mud circulation tanks that combines high efficiency with strong cleaning power.

In the 1950s, Rockwell and Naudascher (1978) systematically investigated cavitation phenomena generated when high-velocity water jets impacted solid surfaces. They discovered that material damage was primarily caused by the immense shock pressure produced during the collapse of these cavitation vortex rings, rather than the steady-state impact pressure of the jet itself. Subsequently, cavitation jets gained widespread attention and were applied in mining,

cleaning, firefighting, and cutting to enhance operational efficiency (Celik and Rockwell, 2002; Zheng et al., 2024; Ji et al., 2016; Wan et al., 2023; Du et al., 2024). Cavitation jet nozzles are primarily classified by mechanism into bypass type, vortex type, self-oscillating pulse type, and central-body type. Bypass-type and vortex-type nozzles exhibit energy dispersion due to the placement of blunt bodies or guide vanes within the flow field, resulting in a lower-pressure peak. Central-body cavitation typically occurs near the central axis, commonly used for rock fragmentation and steel cutting, though with relatively lower cleaning efficiency. Self-oscillating cavitation jets represent the highest cavitation intensity and energy efficiency. This paper focuses on analyzing self-oscillating cavitation jet nozzles, which are capable of cleaning hard deposits.

Commonly used self-oscillating cavitation jet nozzles include organ-pipe-type cavitation jet nozzles and Helmholtz-type cavitation jet nozzles (Li et al., 2016; Yao et al., 2022). Wu et al. (2023) found that organ-pipe-type cavitation jet nozzles have a relatively limited effective operating range and concentrated energy distribution, resulting in lower efficiency for large-area cleaning tasks in recirculation tanks. Han et al. (2017) validated this conclusion through comparative studies of other cavitation jet nozzle types, concluding that Helmholtz-type nozzles exhibit more pronounced self-oscillation resonance frequencies, amplitude values, and peaks. Kolšek et al. (2007) investigated the influence of nozzle structural parameters on self-oscillation frequency via numerical simulation, employing Fourier transform analysis to achieve superior low-frequency self-oscillation characteristics. Liu et al. (2017) proposed a modified theoretical model through simulation, combined numerical modeling to determine the oscillation frequency range, and validated it with experimental results. These studies indicate that the self-oscillation performance of Helmholtz-type cavitation jet nozzles is influenced by their structural parameters. Zhang et al. (2021) employed numerical simulation to investigate the influence of structural parameters on the cavitation characteristics of Helmholtz-type cavitation jet nozzles. Results indicate that smaller outlet length, resonant cavity diameter, and resonant cavity length generate more cavitation bubbles in the flow fields inside and outside the Helmholtz nozzle, while outlet diameter has a negligible effect on the volumetric fraction of cavitation bubbles. Wang et al. (2005) investigated the influence of structural parameters on the self-excited frequency of Helmholtz-type cavitation jet nozzles through numerical simulations and laboratory experiments, identifying an optimized parameter range for this nozzle structure. Zheng (2024) determined via CFD that the ideal dimensions for a double-cavity nozzle are a resonance cavity length ratio of 0.96 and a cavity diameter ratio of 3, both of which enhance cavitation and jet effects. The literature review indicates that structural parameters significantly influence the jet characteristics of Helmholtz-type cavitation jet nozzles, making the optimization of these parameters using appropriate evaluation metrics practically significant. However, previously optimized Helmholtz-type nozzle structures were predominantly derived from single-parameter analysis or orthogonal design schemes. This study establishes a complete orthogonal system, revealing that past optimization results were confined to local optima. Such structures exhibit limited cleaning efficacy for mud circulation tanks and lack evaluations of jet pulse characteristics under submerged conditions.

To achieve global optimization of self-oscillating cavitation jet nozzles, this paper designs a structural optimization system for such nozzles that addresses multiple variables and objectives. First, an orthogonal design scheme is developed. Through range analysis, structural parameters with significant cumulative effects are selected as key variables for establishing a complete orthogonal system. Cleaning performance metrics also exhibit inconsistent standards. The criteria importance through intercriteria correlation (CRITIC) method assigns weights proportional to their information content to these performance metrics. Subsequently, a discrete optimization space is constructed based on key structural parameters and cleaning performance metrics. A machine learning model maps this discrete space into a continuous optimization domain. Finally, the multi-objective particle swarm optimization (MOPSO) algorithm is employed to search for the Pareto front solution set within the optimization space. The optimal structural parameters are then determined using the technique for order preference by similarity to an ideal solution (TOPSIS) combined with information-based weighting.

The remaining sections are as follows. Section 2 introduces the theoretical basis of self-excited cavitation jets and establishes a simulation model in FLUENT. Section 3 describes the optimization method and presents the corresponding mathematical model. Section 4 analyzes the optimization results and explains the mechanism of flow field changes. Section 5 summarizes the entire paper.

2 Establish a finite-element model

2.1 Fundamental principles

When the jet passes through the outlet of the upper nozzle and flows into the self-resonating chamber, the abrupt change in flow channel geometry causes separation of the wall boundary layer, forming a cavitation zone within the outlet flow path. Numerous cavitation bubbles appear in the jet flowing through this region (see Fig. 1). These cavitation bubbles gradually migrate toward the nozzle outlet with the jet's motion. Their morphology also changes in response to pressure variations within the outlet flow channel. The collapse or fragmentation of cavitation bubbles during this process significantly impacts the jet. By utilizing the self-oscillating pulse effect within a self-oscillating chamber in the nozzle, a periodic cavitation jet can be generated. This

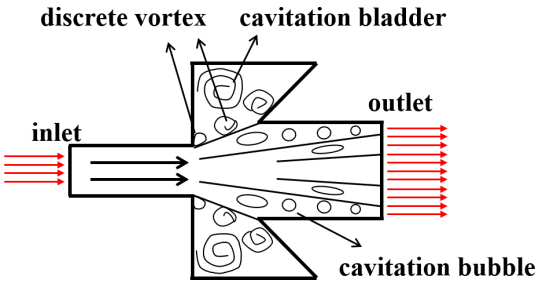

Figure 1. Schematic diagram of self-excited cavitation jet.

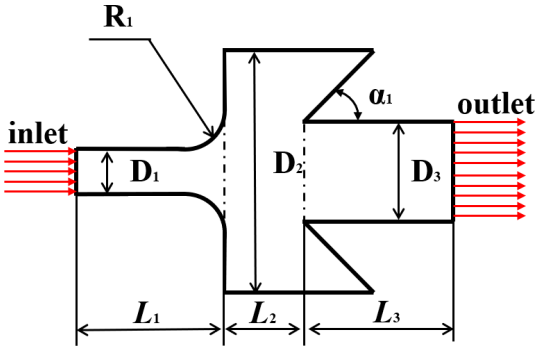

Figure 2. Schematic diagram of self-excited cavitation jet.

achieves periodic energy accumulation and release on the inflow at the nozzle inlet, transforming the continuous jet into a pulsed jet. This technology replaces the "continuous scouring" of traditional water jets with "high-frequency hammering", addressing numerous pain points in mud tank cleaning. These include incomplete cleaning and extremely adhesive and hardened deposits such as mud cakes and solidified cement on tank walls and components.

2.2 Geometric models

Yuan et al. (2024) experimentally verified that jet fields with symmetric characteristics can be computed by simplifying them into two-dimensional models. To reduce computational complexity, this paper also adopts the aforementioned method for numerical simulation. The geometric model of the self-oscillating cavitation jet nozzle selected for this study is shown in Fig. 2. Structural parameters include the upper-nozzle diameter D_1, upper-flow channel length L_1, inlet radius R_1, cavity diameter D_2, cavity length L_2, collision wall angle α_1, lower-flow channel length L_3, and lower-nozzle diameter D_3.

2.3 Setup of boundary conditions and governing equations

Assuming water is an incompressible fluid and neglecting the effect of temperature on the flow field, the fluid flow is considered isothermal. The simulation employs a transient simulation structure with a pressure solver. The inlet pressure is set at 5 MPa, while the outlet pressure simulates a submerged environment at a depth of 1 m with a gauge pressure of 9800 Pa, representing the conditions at the bottom of the mud circulation tank. With a boundary layer mesh size of 0.2 mm, the computational step size is determined as 10^{-5} based on empirical formulas (Yuan et al., 2024). The mixture multiphase flow model was selected, with the realizable k–ε turbulence model, standard wall function for wall conditions, and Schnerr and Sauer cavitation model. The first phase was set as liquid water and the second phase as water vapor. Numerical simulations were performed for the flow conditions inside and outside the nozzle. The pressure–velocity coupling scheme employed the pressure-implicit with splitting of operators algorithm. To ensure computational accuracy, a double-precision solver was utilized. The computational domain models for the inlet, outlet, and target plate are illustrated in Fig. 3.

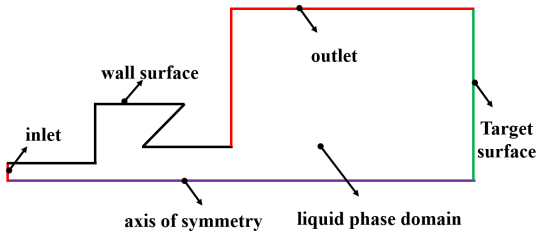

Figure 3. Schematic diagram of boundary condition setup for finite-element model.

2.4 Grid-independent verification and finite-element model correctness verification

The model mesh primarily employs quadrilateral elements. Due to factors such as the small structural dimensions of the nozzle self-excited resonance chamber, cavitation phase transitions, and turbulent vortices, the mesh requires refinement. Using pressure peak (PP) and pressure amplitude (PA) as mesh independence metrics, multiple tests were conducted with meshes of varying refinement levels. Results showed that when the number of mesh elements exceeded 19 788, the differences in pressure peak and pressure amplitude fluctuated within 1 %. This indicates the mesh sufficiently satisfies independence requirements at this level. To validate the model's governing equations and boundary conditions, the simulation replicated the experiment from Li et al. (2024). The comparison revealed less than 5 % deviation between the center of the upper-nozzle flow channel and the outlet jet angle, indicating no significant discrepancy and confirming the correctness of the model parameters.

Table 1. Orthogonal test factor level table.

Factor	R_1 (mm)	D_2 (mm)	L_1 (mm)	D_3 (mm)
1	0.00	4.40	4.00	14.00
2	0.50	4.80	6.00	18.00
3	1.00	5.20	8.00	22.00
4	1.50	5.60	10.00	26.00
5	2.00	6.00	12.00	30.00

3 System design for optimizing the structure of self-excited pulsed cavitation jet nozzles

3.1 Orthogonal design approach

To identify the optimal combination of factors influencing key metrics with the fewest possible trials, an orthogonal test was designed for nozzle structural parameters. This method aims to pinpoint the critical parameters affecting final pressure and frequency. Through investigation, this study found that the nozzle inlet radius R_1, cavity diameter D_2, upper-flow channel length L_1, and lower-nozzle diameter D_3 are more representative than other parameters. Therefore, these structural parameters were selected as optimization variables. The PP, PA, and pressure frequency (PF) of the self-oscillating cavitation jet nozzle are key indicators for evaluating its cleaning performance (Yuan et al., 2024; Li et al., 2024). This design of cleaning performance indicators allows for rapid prediction of cleaning effectiveness through controllable dynamic parameters, facilitating design optimization and operating condition matching. Table 1 lists the values for the four key structural parameters. In Sect. 3.1, Table 2 presents the 25 specific design combinations formed by pairing the five parameters in Table 1, along with their simulation results.

3.2 Development of an evaluation framework based on CRITIC

Direct range analysis would result in each indicator yielding an optimal solution, thus failing to achieve the goal of designing an overall optimal structure. Considering the varying information content within these indicators, the CRITIC weighting method assigns equal weights to the PP, PA, and PF based on their respective information content. These are then combined through linear weighting into a single comprehensive performance indicator, referred to as the cleaning performance indicator (CPI). The steps for the CRITIC weighting method are as follows (Gao et al., 2025):

1. The evaluation matrix **A** is obtained from the orthogonal solution (in Sect. 3.1):

$$\mathbf{A} = \begin{pmatrix} a_{11} & \cdots & a_{1n} \\ \vdots & \ddots & \vdots \\ a_{m1} & \cdots & a_{mn} \end{pmatrix}, \tag{1}$$

where a_{mn} denotes the nth evaluation indicator in the mth sample.

2. Normalize all indicators to obtain the evaluation matrix **B**, ensuring that larger values indicate better performance.

3. Calculate the Pearson correlation coefficients for each indicator:

$$\boldsymbol{r_{k1}} = \frac{\sum_{i=1}^{m}\left(b_{ik}-\overline{b}_k\right)\left(b_{i1}-\overline{b}_1\right)}{\sqrt{\sum_{i=1}^{m}\left(b_{ik}-\overline{b}_k\right)^2}\sqrt{\sum_{i=1}^{m}\left(b_{i1}-\overline{b}_1\right)^2}}, \tag{2}$$

where r_{k1} denotes the correlation coefficient matrix between indicator k and indicator 1, and $\overline{b}_k$ and $\overline{b}_1$ represent the normalized mean values of the kth and ith indicators in the normalization matrix **B**, respectively.

4. The independent coefficient IC_j for the jth evaluation indicator can be expressed as

$$\mathrm{IC}_j = \sum_{i=1}^{m}\left(1-r_{ij}\right). \tag{3}$$

5. Standard deviation is used to quantify the degree of variation in indicator values. The coefficient of variation VC_j for samples under the jth indicator is defined as

$$\mathrm{VC}_j = \sqrt{\frac{\sum_{i=1}^{m}\left(b_{ij}-\overline{b}_j\right)^2}{m-1}}. \tag{4}$$

6. Calculate the information content VOI_j of the jth indicator as

$$\mathrm{VOI}_j = \mathrm{VC}_j \cdot \mathrm{IC}_j. \tag{5}$$

7. Calculate the weight w_j for the jth indicator as

$$w_j = \frac{\mathrm{VOI}_j}{\sum_{j=1}^{n}\mathrm{VOI}_j}. \tag{6}$$

8. Calculate the CPI as

$$\mathrm{CPI} = \sum_{j=1}^{n} w_j b_{ij}. \tag{7}$$

Equation (7) presents the method for weighting the three cleaning indicators according to their information content.

3.3 Constructing the continuous optimization space

Assuming the optimization problem requires 100 iterations, each simulating 50 scenarios, the complete iterative process necessitates 5000 calculations in FLUENT, with an estimated computational time of approximately 209 d. This is practically unfeasible under the current experimental setup. Therefore, this study proposes mapping the discrete optimization

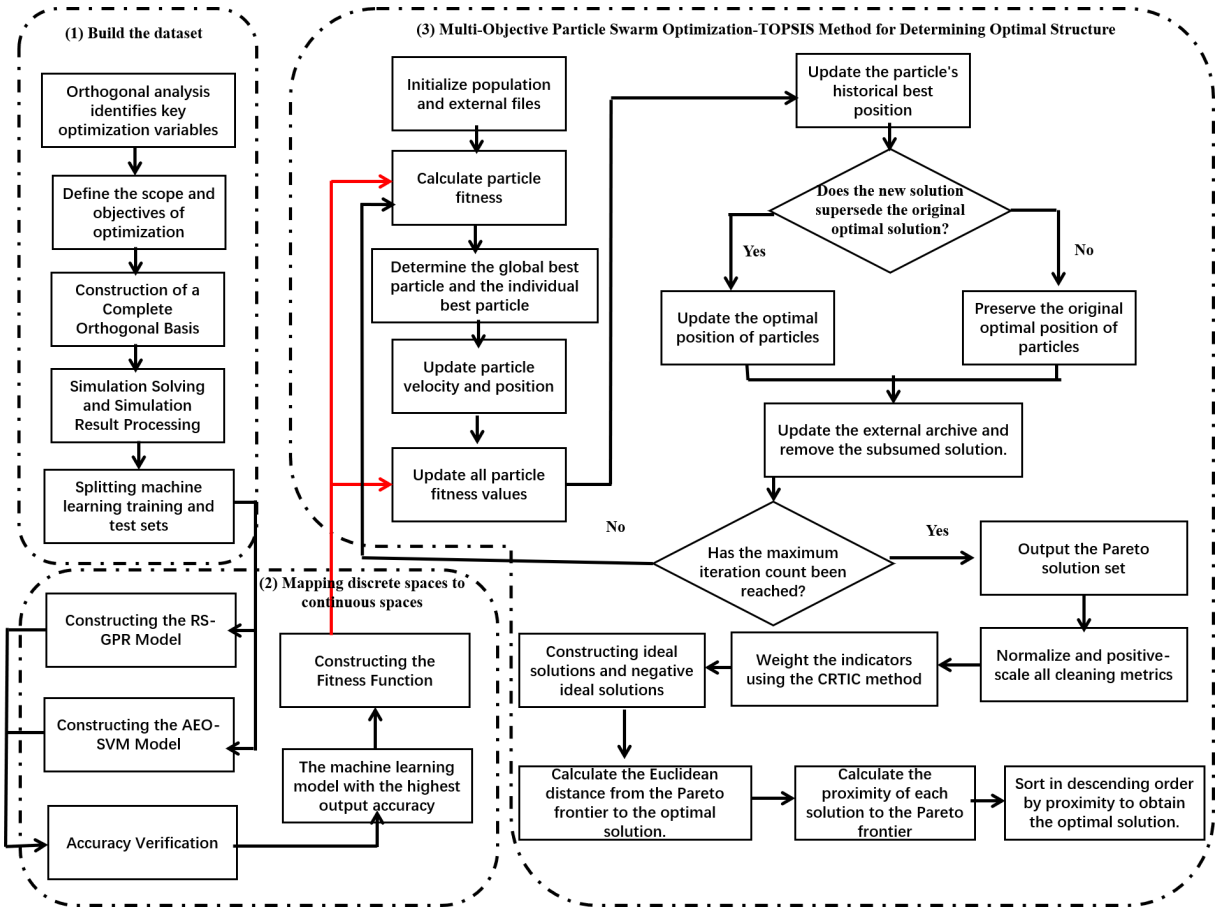

Figure 4. Schematic diagram of a multi-objective optimization system.

space to a continuous optimization space using a Gaussian process regression model to reduce computational time. Key structural parameters serve as input variables to predict three comprehensive cleaning performance metrics: PP, PA, and PF.

The fundamental principle of Gaussian process regression models is the assumption that input data follow a Gaussian distribution, with the relationship between input and output data described by a covariance function (Huang et al., 2023). The covariance function can derive the mean and variance of the output corresponding to any input data, enabling data prediction. The conjugate gradient search method of the model exhibits strong dependence on the initial value σ of the Gaussian kernel function. This paper employs random search to obtain the initial value σ, and this combined model is referred to as the random search Gaussian process regression (RS-GPR) model.

3.4 Multi-objective optimization mathematical models and their solution methods

Minimizing objective functions is generally more conducive to achieving stable convergence than maximizing them. However, since all three cleaning metrics follow a "larger-is-better" pattern, the reciprocals of the three comprehensive cleaning metrics are proposed as the optimization objective function. To prevent zero denominators, an infinitesimal non-zero value (eps) is added to each denominator. The resulting mathematical formulation of the optimization model is as follows:

$$F(f_1, f_2, f_3) = \begin{cases} f_1 = 1/\mathrm{FP} = \\ 1/(\mathrm{RS-GPR_{PP}}(R_1, D_2, L_1) + \mathrm{eps}) \\ f_2 = 1/\mathrm{FA} = \\ 1/(\mathrm{RS-GPR_{PA}}(R_1, D_2, L_1) + \mathrm{eps}) \\ f_3 = 1/\mathrm{FF} = \\ 1/(\mathrm{RS-GPR_{PF}}(R_1, D_2, L_1) + \mathrm{eps}), \end{cases} \quad (8)$$
$$s.t: R_1 \in [0.0,\ 2.0]$$
$$D_2 \in [4.4,\ 6.0]$$
$$L_1 \in [4.0,\ 12.0],$$

where F represents the objective function to be optimized, f_1 minimizes the PP indicator, f_2 minimizes the pressure amplitude PA indicator, f_3 minimizes the PF indicator, RS-GPR$_{\mathrm{PP}}$ denotes the Gaussian regression model for predicting the PP indicator, RS-GPR$_{\mathrm{PA}}$ denotes the Gaussian regression model for predicting the PA indicator, and RS-GPR$_{\mathrm{PF}}$ denotes the Gaussian regression model for predicting the PF indicator.

Table 2. Orthogonal experiments and simulation results.

Number	R_1 (mm)	D_2 (mm)	L_1 (mm)	D_3 (mm)	PP (MPa)	PA (MPa)	PF (Hz)
1	0.00	5.20	12.00	18.00	0.67	0.01	1.00
2	0.00	6.00	10.00	22.00	0.81	0.03	1.00
3	0.00	4.40	4.00	14.00	2.40	1.25	1.00
4	0.00	4.80	8.00	26.00	1.39	0.00	1.00
5	0.00	5.60	6.00	30.00	0.95	0.03	1.00
6	0.50	4.80	10.00	18.00	1.37	0.71	625.00
7	0.50	5.60	8.00	22.00	4.19	1.73	714.29
8	0.50	4.40	6.00	26.00	3.03	0.00	1.00
9	0.50	6.00	12.00	14.00	1.19	0.46	454.55
10	0.50	5.20	4.00	30.00	1.93	0.00	1.00
11	1.00	5.60	10.00	14.00	1.87	0.03	416.67
12	1.00	6.00	4.00	26.00	3.27	0.17	1666.67
13	1.00	4.40	8.00	18.00	2.44	0.00	1.00
14	1.00	4.80	12.00	30.00	1.20	0.56	333.33
15	1.00	5.20	6.00	22.00	2.81	0.00	1.00
16	1.50	5.20	8.00	14.00	1.94	0.65	500.00
17	1.50	6.00	6.00	18.00	2.81	0.06	555.56
18	1.50	5.60	12.00	26.00	1.08	0.36	370.37
19	1.50	4.80	4.00	22.00	2.19	0.00	1.00
20	1.50	4.40	10.00	30.00	1.68	0.00	1.00
21	2.00	4.80	6.00	14.00	2.26	0.00	1.00
22	2.00	5.60	4.00	18.00	2.69	0.00	1.00
23	2.00	5.20	10.00	26.00	1.71	0.03	1.00
24	2.00	6.00	8.00	30.00	2.55	0.62	588.24
25	2.00	4.40	12.00	22.00	0.83	0.12	1.00

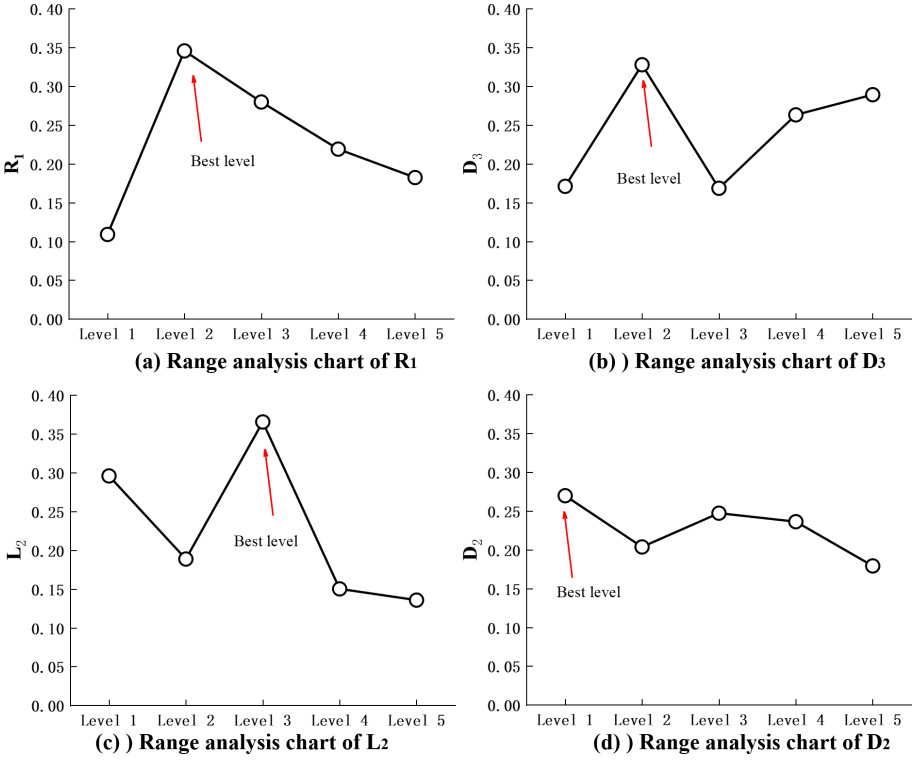

Figure 5. Range analysis chart for different factors.

MOPSO is a well-established approach for solving multi-objective optimization problems and has been applied to optimization tasks in various fields, such as robot pose estimation and power grid scheduling (Lu et al., 2025; Nagayo et al., 2025). The MOPSO algorithm employs 200 spatial particles, stores 200 optimal solutions, and operates with a maximum iteration count of 500. The inertia weight is set to 0.4, with both individual and population cognitive variables configured at 2. Each dimension utilizes 20 grid points, and the mutation probability is 0.5.

3.5 Optimal multi-objective decision evaluation method based on TOPSIS

The TOPSIS method selects a compromise solution that is both closest to the positive ideal solution and farthest from the negative ideal solution by calculating the Euclidean distances between the solutions in the Pareto front and the positive and negative ideal solutions. The steps of the TOPSIS method are as follows:

1. Normalize the objective function values on the Pareto frontier boundary and assign weights w to obtain the decision matrix $\mathbf{C}$:

$$\mathbf{C} = (x_{i,j})_{200\times 3}\boldsymbol{\omega} = \begin{bmatrix} x_{1,1} & x_{1,2} & x_{1,3} \\ x_{2,1} & x_{2,2} & x_{2,3} \\ \cdots & \cdots & \cdots \\ x_{200,1} & x_{200,2} & x_{200,3} \end{bmatrix}\boldsymbol{\omega}, \quad (9)$$

where $x_{i,j}$ denotes the jth evaluation metric in the ith exciter structure scheme. Here, $j = 1, 2, 3$ corresponds to PP, PA, and PF, respectively, and w is calculated by the CRITIC method.

2. Define two ideal solutions: the positive ideal solution for the jth composite indicator is C_j^+, and the negative ideal solution is C_j^-:

$$C_j^+ = \max\left(C_{i,j}\right) i \in [1, 200], j \in [1, 3], \quad (10)$$

$$C_j^- = \min\left(C_{i,j}\right) i \in [1, 200], j \in [1, 3]. \quad (11)$$

3. Calculate the Euclidean distance between the Pareto frontier and the optimal solution:

$$D_i^+ = \sqrt{\sum_{i=1}^{3}\left(C_{ij} - C_j^+\right)^2}\, i \in [1, 200], j \in [1, 3], \quad (12)$$

$$D_i^- = \sqrt{\sum_{i=1}^{3}\left(C_{ij} - C_j^-\right)^2}\, i \in [1, 200], j \in [1, 3]. \quad (13)$$

Here D_i^+ and D_i^- represent the distances between the evaluation object i and the positive ideal solution and negative ideal solution, respectively.

Table 3. Calculation results of comprehensive indicator information content.

Indicator	IC	VC	VOI	w
PP (MPa)	1.2728	0.2513	0.3198	0.3394
PA (MPa)	1.2892	0.2561	0.3302	0.3504
PF (Hz)	1.2477	0.2343	0.2923	0.3102

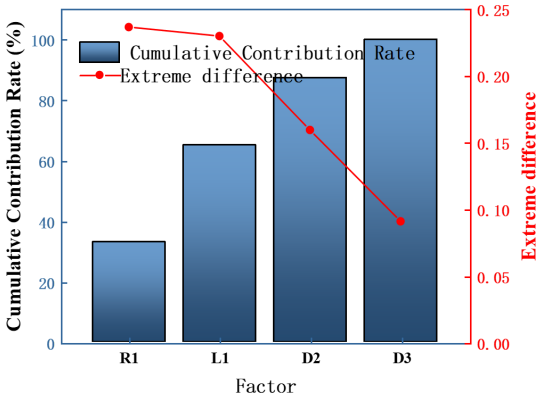

Figure 6. Contribution plot of range for each factor.

4. Calculate the proximity score E_i for evaluation object i:

$$E_i = \frac{D_i^-}{D_i^+ + D_i^-}. \quad (14)$$

5. Rank the Pareto front based on E_i (hereafter referred to as the comprehensive cleaning effect). The scheme with the highest comprehensive cleaning effect, E_i, represents the optimal configuration for the self-oscillating jet nozzle structure parameters.

3.6 Optimal multi-objective decision evaluation method based on TOPSIS

An orthonormal basis for the key structural parameters (R_1, D_3, and L_2) is constructed, and the target values (PP, PA, and PF) for each orthonormal basis scheme are computed through simulations to establish a discrete optimization space. Subsequently, RS-GPR and AEO-SVM models are developed to map the discrete optimization space into a continuous optimization space, with the highest-accuracy model selected as the fitness function for subsequent multi-objective optimization calculations. The MOPSO algorithm is then employed to identify the Pareto front solution set within the machine-learning-constructed continuous optimization space. Finally, the Euclidean distances between the Pareto front solutions and the ideal solution are computed using the TOPSIS method. By ranking these Euclidean distances, the globally optimal solution is determined. The overall optimization workflow is illustrated in Fig. 4.

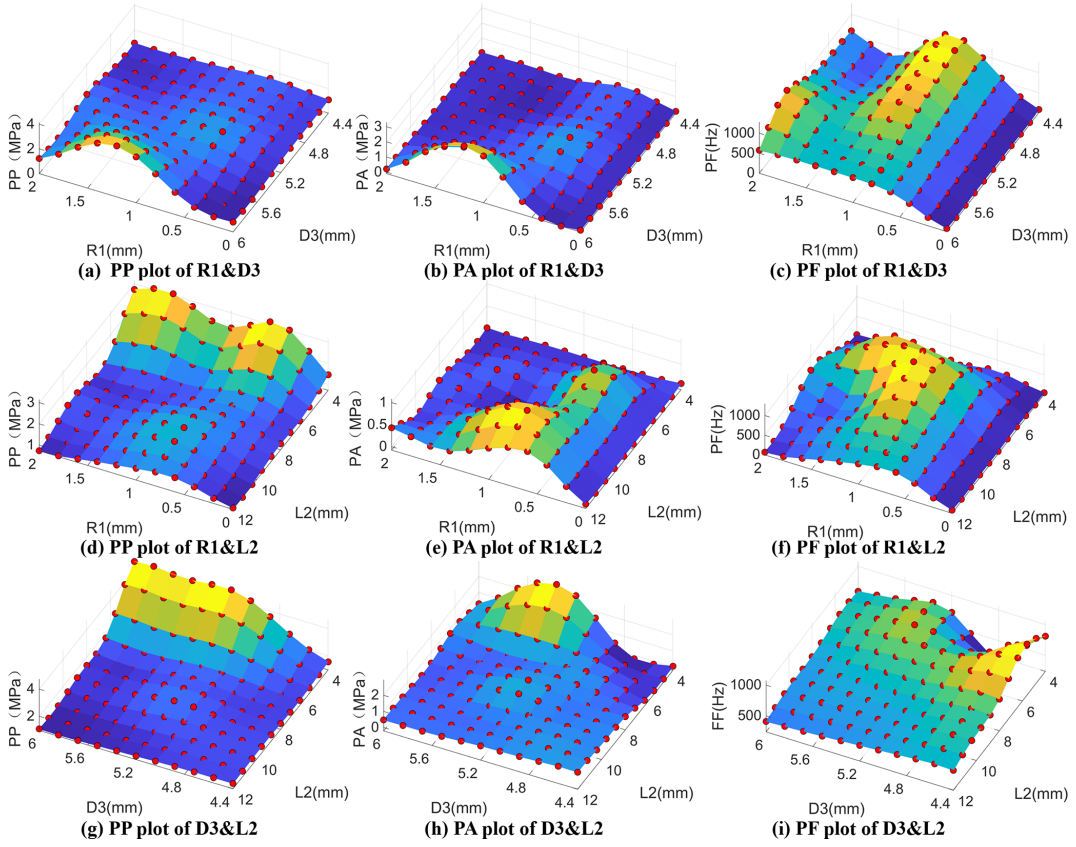

Figure 7. Response surface diagram for different structural parameters.

4 Analysis of optimization results

4.1 Orthogonal results analysis

An orthogonal test matrix for the nozzle was established, and various cleaning indicators were calculated through simulation, as shown in Table 2. Through range analysis, the optimal matching scheme for structural parameters can be obtained when the three cleaning indicators (PP, PA, and PF) achieve their combined optimum.

It should be noted that a frequency value of 1 does not represent one cycle per second, but rather indicates that no complete cycle was detected within the computed 0.5 s time interval. Therefore, the value of 1 is assigned merely as a placeholder. This approach prevents the frequency field from being empty and, due to the normalization of the dataset, will not affect the subsequent optimization calculations.

Applying the CRITIC method to the three evaluation metrics yields Table 3. The PA metric encompasses the largest VOI, contributing 35.04 % to the composite metric. Next is the PP, accounting for 33.94 % of the composite metric. The PF metric covers the minimum VOI, contributing 31.02 % to the composite metric.

Using the CRITIC method, the computationally derived cleaning metrics were first dimensionless and assigned weights proportional to their information content. Range analysis was then applied to these metrics, with the results plotted in Fig. 5.

As shown in Fig. 5, the optimal level for the R_1 is Level 2, the D_2 is Level 2, the self-oscillating cavity length is Level 3, and the self-oscillating cavity diameter is Level 4. Thus, the optimal structural parameter combination obtained through orthogonal analysis combined with the CRITIC weighting method is $R_1 = 0.5$, $D_2 = 4.8$, $L_1 = 8.0$, and $D_3 = 14.0$ mm. Range analysis reveals the contribution rates of the four factors to the comprehensive index, as shown in Fig. 6. They can be ranked by contribution as follows: $R_1 > L_1 > D_2 > D_3$. The top three factors collectively account for approximately 87.36 % of the total contribution rate, while the contribution rate of the self-oscillation cavity diameter is about half that of the third-ranked lower-nozzle diameter; its contribution is relatively minor. The subsequent construction of the complete orthogonal system considers only the inlet fillet radius, self-oscillation chamber length, and lower-nozzle diameter as the key structural parameters.

4.2 Response surface analysis

Using the three key structural parameters analyzed in Sect. 3.4 as optimization variables, a complete orthogonal

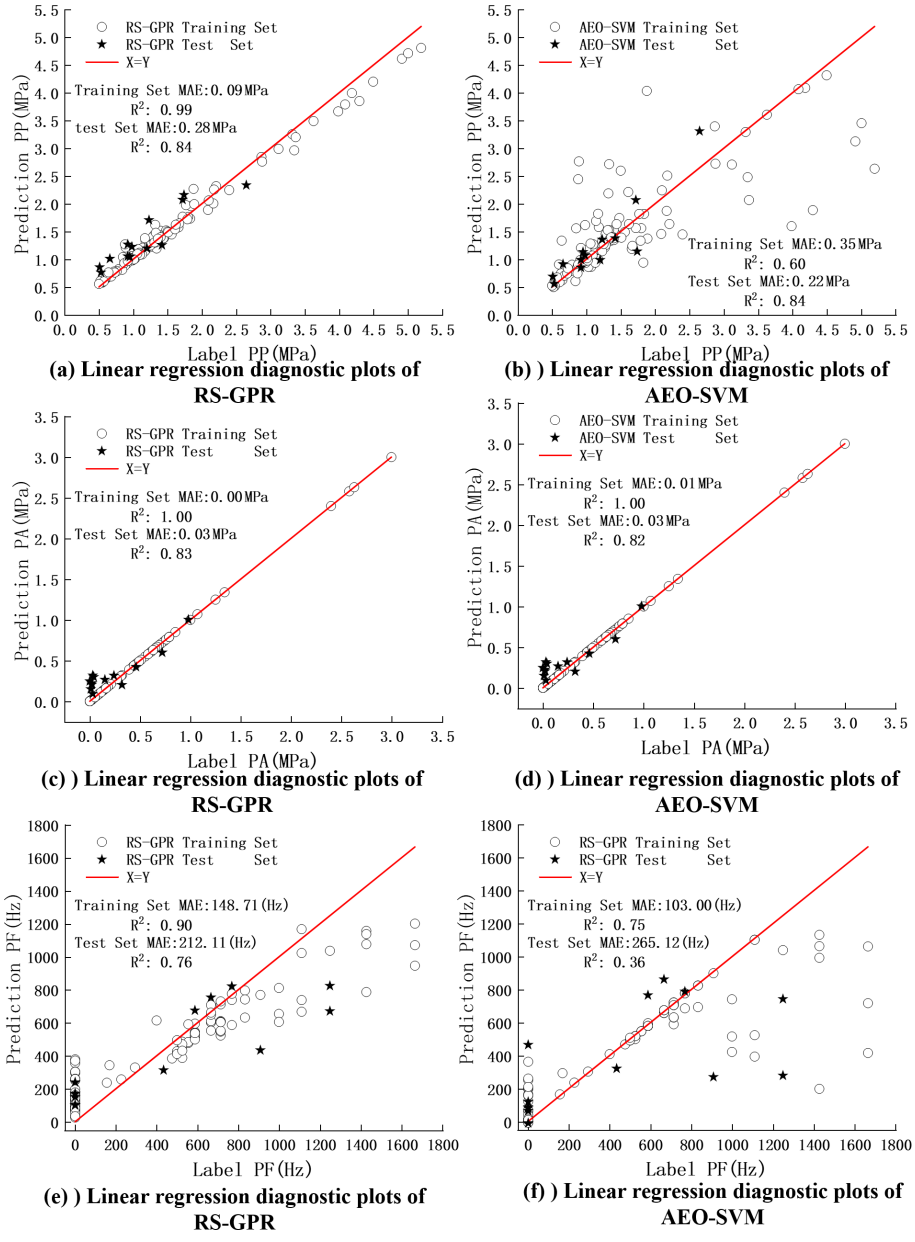

(a) Linear regression diagnostic plots of RS-GPR

(b)) Linear regression diagnostic plots of AEO-SVM

(c)) Linear regression diagnostic plots of RS-GPR

(d)) Linear regression diagnostic plots of AEO-SVM

(e)) Linear regression diagnostic plots of RS-GPR

(f)) Linear regression diagnostic plots of AEO-SVM

Figure 8. Linear regression diagnostic plots for two models.

array was constructed, resulting in 5^3 finite-element simulation cases. Three cleaning metrics were extracted from the computed cases to establish a discrete optimization space. This discrete optimization space enabled the generation of response surfaces for different parameters under various metrics, achieving the goal of visualizing the relationship between different structural parameters and their corresponding metrics.

Figure 7a, d, and g shows the PP response surfaces obtained from the complete orthogonal design. As shown in Fig. 7a, when the nozzle diameter exceeds 5.5 mm, the PP at the inlet fillet exhibits a downward-opening quadratic distribution. In Fig. 7d, the PP gradually increases as the self-oscillating cavity length decreases. In Fig. 7g, larger lower-nozzle diameters and shorter self-oscillating cavity lengths result in higher PP. Figure 7b, e, and h present the PA response surfaces for impact force. As shown in Fig. 7a, the value map closely resembles the peak map, exhibiting a maximum point. In Fig. 7e, the inlet radius forms a downward-opening quadratic relationship with the amplitude. In Fig. 7h, the PA gradually increases as the self-oscillating cavity length decreases. Figure 7c, f, and i presents the response surfaces for the pressure frequency PF. As shown in Fig. 7c, the response surface formed by the inlet fillet and lower-

Table 4. Multi-objective optimization result table.

Case	R_1	D_3	L_2	PP	PA	PF	E_i
Initial solution	0.50	4.80	8.00	1.38	0.61	714.29	0.16
Optimal solution	0.50	5.31	4.20	4.57	2.85	809.54	0.69

nozzle diameter is irregular but generally exhibits the characteristic that the pressure frequency gradually increases as the lower-nozzle diameter decreases. In Fig. 7f, the response surface formed by the inlet radius and the self-oscillating cavity exhibits a maximum point. In Fig. 7i, the overall image shows that the frequency gradually increases as both the lower-nozzle diameter and the self-oscillating cavity length decrease.

In summary, variations in different structural parameters exhibit significant interactive effects on cleaning performance, indicating that global optimization is essential. To establish a continuous optimization space, it is necessary to identify a fitting model capable of effectively characterizing nonlinear interaction effects.

4.3 Mapping the continuous optimization space

Support vector machines (SVMs) are frequently employed in image classification and nonlinear regression tasks. The selection of their hyperparameters – regularization parameters and kernel function parameters – directly impacts the final fitting results. This paper utilizes the artificial ecological optimization (AEO) algorithm to address this issue. The SVM model optimized by the AEO algorithm is subsequently referred to as the AEO-SVM model. This model, along with the RS-GPR model, maps the discrete optimization space into a continuous optimization space. The optimal model among the two is selected to complete subsequent optimization tasks. The kernel functions defined for the AEO-SVM and RS-GPR models are the radial basis function kernel and the Gaussian kernel, respectively.

The model was trained using three key variables as inputs and the PP as the output. The training and testing data for both models were plotted in linear regression diagnostic plots (Fig. 8a–b). The RS-GPR model exhibits a relatively smaller distance from the $X = Y$ line for both training and test data, whereas the AEO-SVM model shows a larger distance. This indicates that the RS-GPR model possesses a stronger capability than the AEO-SVM model in constructing the continuous optimization space for PP. The mean absolute error (MAE) and goodness of fit (R^2) values of the AEO-SVM model show little difference between the training and test sets, indicating that no overfitting or underfitting occurred. In contrast, the AEO-SVM model exhibits clear underfitting characteristics.

The pressure amplitude PA was trained as the model output to generate linear regression diagnostics (Fig. 8c–d). Both models exhibited proximity to the $X = Y$ line in both

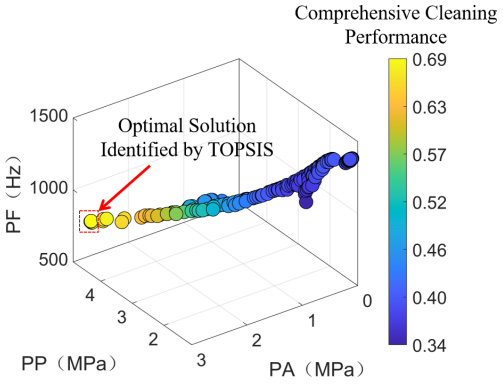

Figure 9. Pareto frontier surface plot.

training and test datasets, nearly forming a straight line. Quantitative metrics MAE and R^2 were also observed: the RS-GPR model demonstrated a 0.01 MPa reduction in training set MAE compared to AEO-SVM, while test set R^2 improved by approximately 0.01. This indicates that the RS-GPR model is slightly superior to the AEO-SVM model. Training the model with the pressure frequency period as the output yields the linear regression diagnostic plots shown in Fig. 8e–f. Both models exhibited poor predictive performance. The RS-GPR model achieved an MAE of 212.11 Hz on the test set, representing a 53.01 Hz reduction compared to the AEO-SVM model. Its R^2 on the test set was 0.76, an improvement of 0.40 over the AEO-SVM model. This demonstrates that the RS-GPR model significantly outperforms the AEO-SVM model in predicting the impact force cycle.

In summary, the RS-GPR model effectively characterizes the nonlinear relationships between structural parameters and various evaluation metrics. Therefore, subsequent studies employ RS-GPR to construct continuous optimization spaces.

4.4 Optimization results and resonance mechanism analysis

The Pareto front solution set obtained by solving within the optimization space constructed by RS-GPR using MOPSO is shown in Fig. 9. As the frequency gradually increases, both the PP and the pressure amplitude decrease. This aligns with practical observations. Considering the limiting case, when the pressure frequency increases to infinity, the pressure amplitude decreases to 0, indicating a water jet state. At this point, the PP remains constant, and no cavitation reaction occurs. Additionally, within the Pareto front solution set, it can be observed that as the PP increases, the pressure amplitude also gradually increases. However, the frequency progressively decreases. This further demonstrates that no solution set exists that simultaneously satisfies all performance metrics.

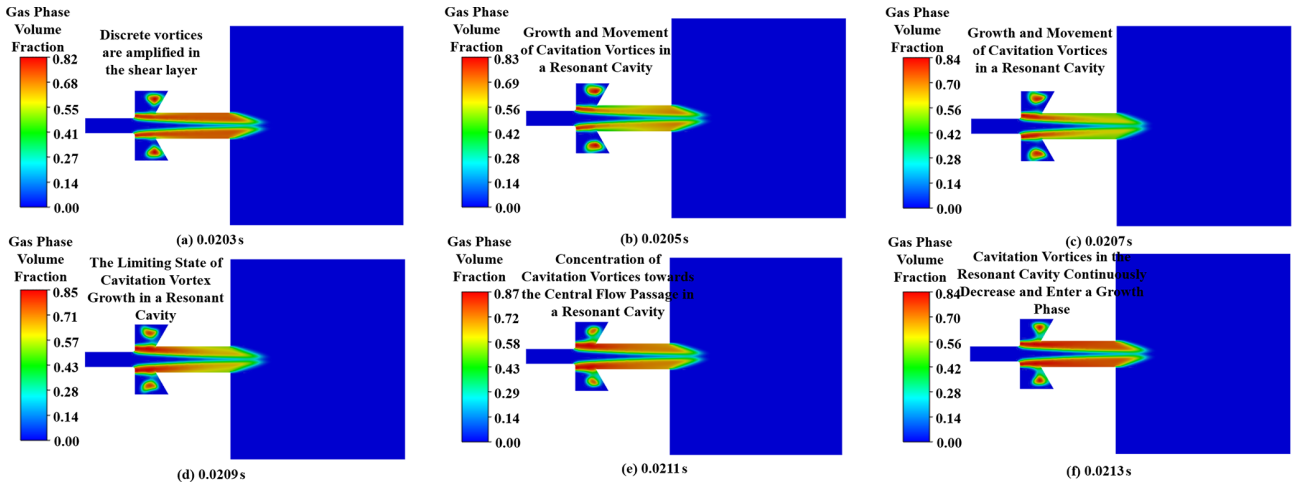

Figure 10. Gas-phase mass fraction diagram.

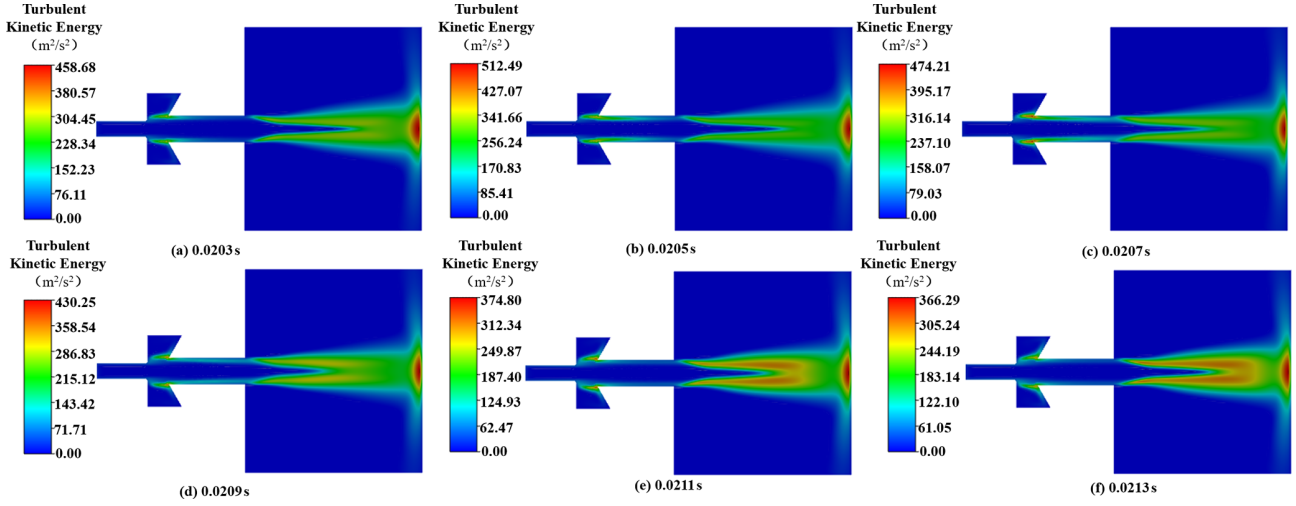

Figure 11. Turbulent kinetic energy diagram.

Table 4 shows the results obtained by calculating the Pareto frontier using the TOPSIS method. Among these, Case 1 represents the solution obtained through orthogonal analysis, while Case 2 represents the solution obtained using the method proposed in this paper (abbreviated as the global optimization solution). The optimal solution with the best comprehensive cleaning performance on the Pareto frontier is 0.69, with a chamfer radius of 0.5 mm, a lower-nozzle diameter of 5.31 mm, and a self-oscillating cavity length of 4.20 mm. The PP during cleaning is 4.57 MPa, the PA is 2.85 MPa, and the frequency is 809.54 Hz. The orthogonal optimization solution's comprehensive cleaning performance was 0.16. Compared to the orthogonal optimization solution, the optimal solution to the method proposed in this paper achieved improvements of 69.79 % in PP, 78.60 % in PA, and 11.77 % in PF. After global optimization, all cleaning metrics of the structural parameters showed significant enhancements over the orthogonal optimization solution, with the comprehensive cleaning performance increasing by 77.39 %.

Figure 10 was obtained by extracting the gas-phase volume fraction map from the simulation results of the optimal structure. Due to the presence of the inlet fillet, strong shear forces exist between the high-speed jet and the stationary fluid medium within the resonant cavity. Significant cavitation occurs at the rounded corners. Due to the strong shear forces, cavitation is elongated along the jet direction, causing the gas mass fraction distribution in this region to exhibit a shape that contracts near the inlet of the self-oscillating cavity and diverges near its outlet. The fixed-angle collision wall at the chamber outlet causes the formed discrete vortices to spontaneously aggregate toward the self-oscillating cavity, as depicted in the growth process shown in Fig. 10a–c. When the cavitation vortex within the resonant cavity evolves to its limit state (as shown in Fig. 10d), it begins migrating toward

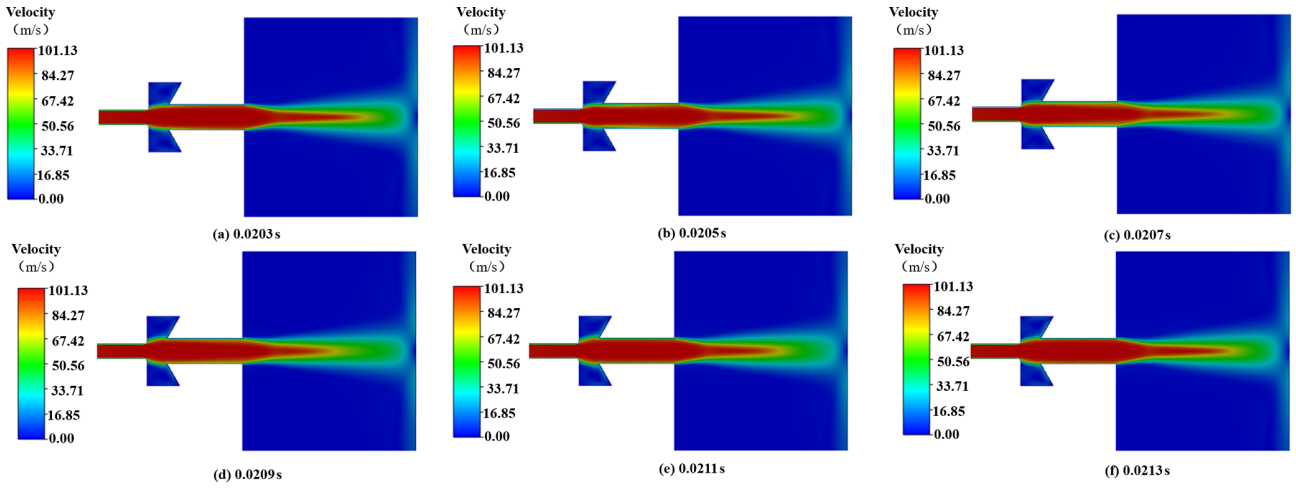

Figure 12. Velocity distribution diagram.

the central flow channel. This displacement compresses the high-velocity jet within the central channel. The substantial energy accumulated in the resonant cavity is instantaneously released. The cavitation vortex continuously shrinks while a large number of cavitation bubbles are ejected along with the jet, forming a pulsed cavitation jet. The energy release process is shown in Fig. 10e–f. After the nozzle completes energy release, the cavitation vortex continues to shrink and moves toward the central region of the resonant cavity, evolving further into the energy accumulation stage.

Figure 11 shows the turbulent kinetic energy distribution contour map of the nozzle flow field at different time points. As shown in the figure, due to intense cavitation phase transitions and complex turbulent motion within the nozzle cavity, a high concentration of turbulent kinetic energy exists around the line connecting the inlet fillet and the collision wall. In the external flow field, the pulsed cavitation jet undergoes intense energy exchange with the liquid phase. A significant velocity gradient exists between the high-speed jet and the stationary liquid medium in the external flow field. Numerous turbulent vortices are present within the shear layer of the external flow field, resulting in high turbulent kinetic energy intensity around the pulsed cavitation jet. During the growth phase of cavitation vortices within the self-oscillating cavity, the turbulent kinetic energy at the target plate is at its maximum. During the release phase of the internal cavitation vortices, the turbulent kinetic energy is at its minimum.

As shown in Fig. 12, these are velocity distribution contour plots of the cavitation jet nozzle flow field at different time points during self-oscillating pulsation. The figure reveals that the inlet nozzle velocity is consistently the highest, with nearly uniform velocity distribution at the nozzle. Between 0.0203 and 0.0209 s, the velocity in the central flow channel of the outer flow field gradually decreases. This period corresponds to the cavitation vortex growth and energy accumulation stages, during which the core region of the jet is relatively short. This state is corroborated by the magnitude of turbulent kinetic energy in Fig. 12. At 0.0211–0.0213 s, the velocity length in the central flow channel of the outer flow field gradually increases. The flow field enters the energy release stage, where the cavitation vortex compresses toward the central flow channel while releasing a large number of cavitation bubbles that move with the main jet, forming a pulsed cavitation jet with extremely strong cleaning effects.

The inner walls and bottom of mud circulation tanks typically accumulate and adhere to substantial deposits of heavy drill cuttings, barite, clay, and other substances. Traditional manual cleaning or ordinary water jet cleaning methods are inefficient, labor-intensive, and pose risks associated with confined space entry. In response to the abundant microjets and shock waves generated during cavitation bubble collapse, the optimized structure developed in this paper demonstrates superior cleaning performance. Meanwhile, it also provides a theoretical basis for the subsequent application of self-excited oscillation cavitating jet nozzles in the cleaning of mud circulation tanks.

5 Conclusions

This paper employs orthogonal analysis to characterize the effects of structural parameters of a self-excited oscillating nozzle on cleaning performance. A multi-objective optimization mathematical model linking structural parameters to cleaning performance is established. The optimal structure is determined using a multi-objective particle swarm optimization algorithm combined with the TOPSIS method, thereby providing an efficient and feasible engineering solution for the automatic cleaning of mud circulation tanks. Key conclusions are as follows:

1. Different combinations of key structural parameters in self-oscillating nozzles produce significant compound

effects on cleaning performance. Orthogonal analysis reveals that the structural parameters affecting cleaning performance, ranked from strongest to weakest, are inlet radius, self-oscillation cavity length, lower-nozzle diameter, and self-oscillation cavity diameter. Among these, the combined influence of inlet radius, lower-nozzle diameter, and self-oscillation cavity length on cleaning performance exceeds 87 %, making them key optimization variables for research.

2. The globally optimal values for inlet radius R_1, lower-nozzle diameter D_3, and cavity length L_2 are 0.50, 5.31, and 4.20 mm, respectively. Compared to the orthogonal analysis structure, the multi-objective optimized structure achieved improvements of 69.79 %, 78.60 %, and 11.77 % in pressure peak, pressure amplitude, and frequency, respectively, with an overall cleaning efficiency enhancement of 77.39 %.

3. The velocity distribution, phase distribution, and turbulent kinetic energy variations within the flow field of the optimal structure were analyzed. The evolution mechanism of the internal and external flow fields in the self-oscillating pulsed cavitation jet nozzle was investigated and explained.

Investigating the direct cleaning performance associated with physical cleaning manifestations in benchmark tests that exhibit strong engineering relevance constitutes the next phase of our team's research plan.

Code availability. Code will be made available on request.

Data availability. Data will be made available on request.

Author contributions. Jinhui Fan: writing – original draft, validation. Peng Hao: writing – original draft, validation. Ke Liu: writing – review and editing, funding acquisition. Yuan Gao: writing – original draft, methodology. Zhang Liang: writing – review and editing, funding acquisition. Changkun He: writing – review and editing. Zhuang Hao: writing – review and editing.

Competing interests. The contact author has declared that none of the authors has any competing interests.

Disclaimer. Publisher's note: Copernicus Publications remains neutral with regard to jurisdictional claims made in the text, published maps, institutional affiliations, or any other geographical representation in this paper. The authors bear the ultimate responsibility for providing appropriate place names. Views expressed in the text are those of the authors and do not necessarily reflect the views of the publisher.

Acknowledgements. This work was supported in part by the CNPC Science and Technology Project (grant no. 2025ZG56).

Financial support. This work was supported in part by the CNPC Science and Technology Project (grant no. 2025ZG56).

Review statement. This paper was edited by Pengyuan Zhao and reviewed by two anonymous referees.

References

Celik, E. and Rockwell, D.: Shear layer oscillation along a perforated surface: A self-excited large-scale instability, Phys. Fluids, 14, 4444–4447, https://doi.org/10.1063/1.1519531, 2002.

Du, M., Xie, H., Han, C., and Yu, K.: Numerical investigation of submerged cavitation jet based on stress-blended eddy simulation, J. Mech. Sci. Technol., 38, 6113–6127, https://doi.org/10.1007/s12206-024-1028-6, 2024.

Fang, Z., Ji, Z., Kang, D., Chen, Y., Zhang, X., Wang, S., and Xiong, T.: Cavitation damage characteristics following marine fouling cleaning by a self-excited oscillation cavitation waterjet, Appl. Ocean Res., 139, 103692, https://doi.org/10.1016/j.apor.2023.103692, 2023.

Gonzalez, M., Thiel, T., Gooneratne, C., Adams, R., Powell, C., Magana-Mora, A., Ramasamy, J., and Deffenbaugh, M.: Development of an In-Tank Tuning Fork Resonator for Automated Viscosity/Density Measurements of Drilling Fluids, IEEE Access, 9, 25703–25715, https://doi.org/10.1109/ACCESS.2021.3050919, 2021.

Gao, Y., Zhang, L., Liang, Z., and Zheng, T.: Multi-objective optimization design and study of electromagnetic exciter structure, Chinese Journal of Scientific Instrument, 46, 235–250, https://doi.org/10.19650/j.cnki.cjsi.J2513871, 2025.

Han, J., Cai, T., Pan, Y., and Ma, F.: Study on jet's characteristics of organ nozzle and helmholtz nozzle, Safety in Coal Mines, 48, 134–137, https://doi.org/10.13347/j.cnki.mkaq.2017.07.036, 2017.

Huang, H., Wang, Y., and Pang, Q.: Analysis and prediction of wind turbine bolts based on GPR method, J. Mech. Sci. Technol., 37, 1–10, https://doi.org/10.1007/s12206-023-0202-6, 2023.

Ji, B., Wang, J., Luo, X., Miyagawa, K., Xiao, L. Z., Long, X., and Tsujimoto, Y.: Numerical simulation of cavitation surge and vortical flows in a diffuser with swirling flow, J. Mech. Sci. Technol., 30, 2507–2514, https://doi.org/10.1007/s12206-016-0511-0, 2016.

Kang, J., Jang, J., Kim, K., Yoo, W., and Lee, J.: Program development on cleaning pattern and performance evaluation for low pressure waterjet, Adv. Mech. Eng., 1–16, https://doi.org/10.1177/1687814020985162, 2021.

Kolšek, T. K. L. U., Jelić, N., and Duhovnik, J.: Numerical study of flow asymmetry and self-sustained jet oscillations in geometrically symmetric cavities, Appl. Math. Model., 31, 2355–2373, https://doi.org/10.1016/j.apm.2006.10.010, 2007.

Li, D., Kang, Y., Ding, X., Wang, X., and Fang, Z.: An experimental investigation on the pressure characteristics of high speed self-resonating pulsed waterjets influenced by feeding

pipe diameter(Article), J. Mech. Sci. Technol., 30, 4997–5007, https://doi.org/10.1007/s12206-016-1019-3, 2016.

Liu, W., Kang, Y., Zhang, M., Wang, X., and Li, D.: Self-sustained oscillation and cavitation characteristics of a jet in a Helmholtz resonator. Int. J. Heat Fluid Fl., 68, 158–172, https://doi.org/10.1016/j.ijheatfluidflow.2017.10.004, 2017.

Li, J., Guo, C., Li, H., Wang, H., and Yang, D.: Numerical simulation on structural optimization of helmholtz cavitation jet nozzle, China Petroleum Machincal, 50, 98–107, https://doi.org/10.16082/j.cnki.issn.1001-4578.2024.10.013, 2024.

Lu, Z., Cui Y., Zhuang L., and Klingauf U.: Development Assurance Level Assignment Based on Multi-Objective Optimization by Using MOPSO in Aircraft and System Development, IEEE T. Aero. Elec. Sys., 61,1–15, https://doi.org/10.1109/TAES.2025.3560937, 2025.

Ma, R., Qi, B., Ling, Y., Li, X., and Zong, Y.: Development and application of flushing fluid used for shale gas and tight gas, proceedings of the international field exploration and development Conference, Wuhan, China, https://doi.org/10.1007/978-981-97-0256-5_20, 2023.

Nagayo, A. M., Singh, R., Dhawan, A., Manjunath, T. C., Qasem, A., and Sharma, K.: Integrating environmental sustainability in construction Time-Cost trade-off for decision-making using hybrid NSGA-III and MOPSO approach, Asian Journal of Civil Engineering, 26, 1527–1542, https://doi.org/10.1007/s42107-025-01265-3, 2025.

Rockwell, D. and Naudascher, E.: Review–Self-Sustaining Oscillations of Flow Past Cavities, J. Fluid. Eng.-T. ASME, 100, 152–165, https://doi.org/10.1115/1.3448624, 1978.

Wan, L., Xiong, J., Cai, J., Wu, S., Kang, Y., and Li, D.: Feasible study on the sustainable and clean application of steel slag for abrasive waterjet machining, J. Clean. Prod., 420, 138378, https://doi.org/10.1016/j.jclepro.2023.138378, 2023.

Wang, X., Jiao, L., and Wang, L.: Numerical simulation of self-exicited oscillation pulsed jet and analysis of parameters' influence, Journal of Zhejiang University, 39, 176–180, https://doi.org/10.3785/j.issn.1008-973X.2005.09.1450, 2005.

Wu, X., Zhang, Y., Xu, Z., Zhao, S., Li, G., Tian, S., Tan, Y., and Peng, K.: Structure optimization of the organ-pipe cavitating nozzle and its erosion ability test on hydrate-bearing sediments, Pet. Sci., 1104–1118, https://doi.org/10.1016/j.petsci.2022.10.010, 2023.

Yao, Y., Wang, H., Fang, Z., and Wang, D.: Experimental study and prediction model of the cleaning effect induced by self-resonating cavitating waterjet, J. Mech. Sci. Technol., 36, 5097–5106, https://doi.org/10.1007/s12206-022-0922-z, 2022.

Yuan, X, Wang, N., Wang, W., Zhang, L., and Zhu, Y.: Research on resonance mechanism and collaborative optimization for the self-excited oscillating pulse cavitation jet nozzle, Journal of Mechanical Engineering, 60, 377–389, https://doi.org/10.3901/JME.2024.16.377, 2024.

Zhang, F., Wei, Y., Xu, Y., and He, K.: Effects of structural pa-rameters of helmholtz nozzle on cavitating jet characteristics, Journal of Integration Technology, 10, 75–84, https://doi.org/10.12146/j.issn.2095-3135.20201103001, 2021.

Zheng, P.: CFD simulation of dual-cavity self-resonating cavitating nozzle, Sadhana-Acad. P. Eng. S., 49, 1–16, https://doi.org/10.1007/s12046-024-02463-6, 2024.